Emergence of interface states in graphene/transition metal dichalcogenide heterostructures with lateral interface

Zahra Khatibi
School of Physics, Trinity College Dublin, Dublin 2, Ireland

Stephen R. Power*
School of Physical Sciences, Dublin City University, Dublin 9, Ireland
and School of Physics, Trinity College Dublin, Dublin 2, Ireland

(Received 12 April 2023; revised 6 July 2023; accepted 10 July 2023; published 20 July 2023)

The relative strength of different proximity spin-orbit couplings in graphene on transition metal dichalcogenides (TMDCs) can be tuned via the metal composition in the TMDC layer. While Gr/$MoSe_2$ has a normal gap, proximity to WSe_2 instead leads to valley-Zeeman-driven inverted bands. Although the $\mathbb{Z}_2$ index vanishes, these systems enable a concentration-dependent topological crossover with band gap closure when graphene is stacked on a composite or alloyed TMDC layer. This is due to a nonzero Berry curvature at the individual valleys, i.e., a hallmark of the quantum valley Hall effect and a change in the valley Chern index at a critical composition ratio. Therefore, inherently, we also expect that stacked heterostructures of graphene on composite TMDC layers should host localized boundary modes due to the presence of Gr/WSe_2- and Gr/$MoSe_2$-like domains with opposite valley Chern indices. In this study, we show that a Gr/(Mo-W)Se_2 heterostructure with a lateral interface in the TMDC layer can indeed host valley-dependent topologically protected in-gap propagating modes, similar to those at the border of commensurate AB and BA domains in biased minimally-twisted bilayer graphene. However, the stability of these modes depends crucially on the system size. We demonstrate that the electronic behavior of Gr/(Mo-W)Se_2 heterostructures evolves from a homogeneous effective medium to a superposition of domain-localized bands and zero-energy branch crossings as the domain size in the alloyed TMDC layer is increased.

DOI: 10.1103/PhysRevB.108.035415

I. INTRODUCTION

Graphene-based systems with broken inversion symmetry host long-sought topologically protected helical (TPH) states [1–9]. For instance, twisted bilayer graphene has recently received renewed interest for hosting the quantum valley Hall effect (QVHE) and the realization of one-dimensional topological modes. These transport channels emerge in long-range moiré structures of twisted bilayer graphene where a network of domain walls forms between commensurate AB and BA stacking regions [10–14]. An external electric field lifts the inversion symmetry, giving rise to nonzero Berry curvature within and TPH states along the spatially varying stacking registries [15]. Similar localized subgap states have been shown to emerge in a uniform bilayer and, later, in chirally stacked N layers, with opposite polarity-gate domains [16,17]. In fact, the low-energy effective Hamiltonian of multilayer graphene under a uniform vertical electric field has a finite Chern number $(1/2)$ per spin with an opposite sign in each valley [18]. The valley-projected Chern index changes sign over a boundary between domains with opposite polarity, imposing a band gap closure and the emergence of *valley* helical edge states. Overall, dictated by the valley Chern index (i.e., $C_V = C_K - C_{K'}$, the difference between the valley-projected Chern indices), the local boundary states consist of N branches of interface states in chirally stacked N-layer graphene with opposite polarity-gate domains.

Exotic states with built-in spin and valley properties are also predicted to emerge in graphene when spin-orbit interactions are included. With enhanced homogeneous Kane-Mele, or "intrinsic" spin-orbit coupling (SOC), a quantum spin Hall edge state emerges near charge neutrality [19]. This topologically protected edge state consists of counterpropagating channels with opposite spins [20]. Proximity effects induced in graphene by transition metal dichalcogenides (TMDCs) can also generate different quantum Hall effects [21–34]. These effects are rather complex and involve an interplay between a diverse range of sublattice-dependent intrinsic, or "valley Zeeman" (VZ), and Rashba-type SOCs [35–41]. The Rashba term couples electrons of different spin orientations, introducing in-plane spin precession effects in the absence of external magnetic fields [42–45]. Although the staggered nature of the Kane-Mele term in proximitized graphene leads to a trivial topological order [46,47], the nonzero Berry curvature in individual valleys enables a topological interpretation of the electronic structure in graphene on TMDCs [48]. For instance, the band-inverted regime in Gr/WSe_2, where the VZ term dominates, enables the formation of topologically protected pseudohelical edge modes in finite-sized ribbons analogous to those of quantum spin Hall states [47]. Recent studies also suggest the emergence of a pair of interface states per valley in

*stephen.r.power@dcu.ie

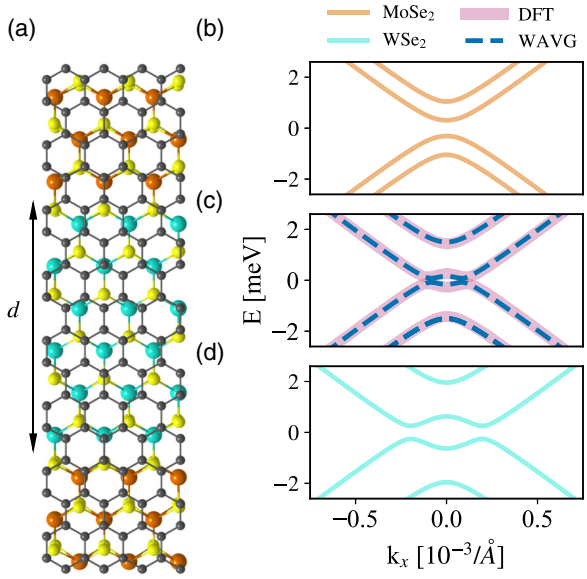

FIG. 1. (a) DFT cell of a Gr/(Mo-W)Se_2 heterostructure with lateral interfaces in the TMDC layer. Tungsten, molybdenum, and carbon atoms are indicated by cyan, orange, and black spheres. The cell is equally divided into two Gr/$MoSe_2$ and Gr/WSe_2 regions. The interfaces between the W- and Mo-like regions are aligned with the zigzag direction. Electronic dispersion of pristine (b) Gr/$MoSe_2$ and (d) Gr/WSe_2 heterostructures. (c) DFT (solid lines) and homogeneous WAVG model bands (dashed lines) energy dispersion of the Gr/(Mo-W)Se_2 heterostructure shown in (a) near the K valley.

proximitized graphene where the VZ term changes sign [49]. The interplay of changing sign VZ and constant Rashba SOCs in graphene can be mapped to stacking registry domains in bilayer graphene where valley-dependent topological channels were previously shown to exist [50,51].

Previously, we showed that proximity spin-orbit coupling in graphene on TMDCs can be controlled via the metal composition in the TMDC layer [52]. In a composite heterostructure, the electronic dispersion resembles a uniform Gr/TMDC system with a weighted average of the SOC parameters of the pure systems, i.e., the weighted average (WAVG) model bands. Particularly, in the case of a composite Gr/$W_\chi Mo_{1-\chi}Se_2$ system, where χ denotes the tungsten-molybdenum ratio, the change in the valley Chern index over the critical composition ratio $\chi = 0.33$ leads to band gap closure and a topological transition. This is because the individual Gr/$MoSe_2$ and Gr/WSe_2 systems host direct and inverted band regimes, respectively, due to the relative strengths of the mass and VZ terms [see Figs. 1(b) and 1(d)]. Therefore, a crossover in the magnitudes of the two terms can lead to a topological crossover in the composite system [52]. We should also therefore expect composite Gr/TMDC heterostructures to host localized boundary states where domains with opposite valley Chern indices are formed. This corresponds, in our case, to a Gr/(Mo-W)Se_2 heterostructure with a lateral interface in the TMDC layer. The crossover between the two unequal valley Chern indices occurs at the border of the Gr/$MoSe_2$ and Gr/WSe_2 domains where the direct and inverted band regimes meet.

In this study, using the tight-binding (TB) model, we investigate the emergence of TPH states in Gr/TMDC heterostructures at the border of the broad $MoSe_2$ and WSe_2. We observe a behavior similar to the case of bilayer graphene with different stacking registries or polarity-gate domains, where the topological branch crossing leads to band gap closure and the emergence of zero-energy modes. Previous studies showed that the boundary modes emerge only in twisted bilayer graphene with remarkably small twist angles where large wavelength moiré patterns form [10,11,15]. Similarly, here, we show that the presence of the interface modes is closely tied to the Gr/$MoSe_2$ and Gr/WSe_2 domain size. We find that in order for zero-energy branch crossings to emerge, the domain size should be comparable to Fermi wavelength, $\lambda_F \approx hv_F/E$, where E is the energy scale of the system. Our findings are experimentally viable with recent advances in the large-scale fabrication and characterization of lateral TMDC heterostructures via controlled alloying [53–58] and chalcogen monomer feeding techniques [59]. Consequently, this suggests deliberate alloying and patterning of the TMDC layer are an effective mechanism for tuning the topological behavior of graphene and the realization of topologically protected transport channels for spintronic applications.

This paper is organized as follows: In Sec. II, we discuss the details of our TB model and the geometry of the system. In Sec. III, we present the density functional theory (DFT) calculated electronic structure and look for signatures of interface states in the band dispersion. Next, we investigate the size effects on the localized interface states in Sec. IV and find the critical system size for a realistic Gr/(Mo-W)Se_2 heterostructure that supports the formation of well-defined boundary modes. In Sec. V, we focus on the detailed properties of interface modes and their evolution with system size. Finally, we conclude our findings in Sec. VI.

II. MODEL

To study the interface states we start with the TB Hamiltonian of p_z orbitals in a graphene layer on a TMDC layer [36,60]:

$$\begin{aligned}\mathcal{H} = &\sum_{\langle i,j\rangle,\sigma} t\, c^\dagger_{i\sigma} c_{j\sigma} + \sum_{i,\sigma} \Delta\, \xi_{c_i}\, c^\dagger_{i\sigma} c_{i\sigma} \\ &+ \frac{2i}{3} \sum_{\langle i,j\rangle} \sum_{\sigma,\sigma'} c^\dagger_{i\sigma} c_{j\sigma'} \left[\lambda_{\mathrm{R}}^{ij} (\hat{\mathbf{s}} \times \mathbf{d}_{ij})_z\right]_{\sigma\sigma'} \\ &+ \frac{i}{3} \sum_{\langle\langle i,j\rangle\rangle} \sum_{\sigma,\sigma'} c^\dagger_{i\sigma} c_{j\sigma'} \left[\frac{\tilde{\lambda}_{\mathrm{I}}^{ij}}{\sqrt{3}} \nu_{ij} \hat{s}_z\right]_{\sigma\sigma'}. \end{aligned} \tag{1}$$

Here, the $c^\dagger_{i\sigma}$ ($c_{i\sigma}$) operator creates (annihilates) an electron at atomic site i with spin σ. $\xi_{c_i} = \pm 1$ is a sublattice index, and $\hat{s}$ is the spin vector made of Pauli matrices. $\mathbf{d}_{ij}$ is the unit vector connecting the nearest neighbors, and $\nu_{ij} = 1\,(-1)$ defines the trajectory sign, i.e., clockwise (counterclockwise) from site j to site i. t is the spin-independent hopping, and Δ denotes the mass term. λ_{R} is the Rashba coupling, i.e., a substrate-induced SOC due to symmetry breaking in the transverse direction that introduces in-plane spin textures. $\tilde{\lambda}_{\mathrm{I}}$ is a generic sublattice-dependent intrinsic parameter that can be written in terms of

TABLE I. Calculated orbital and spin-orbit parameters of graphene in Gr/TMDC heterostructures, found by fitting DFT results to a continuum Dirac model. t is the nearest-neighbor tunneling energy, Δ is the proximity-induced orbital gap, λ_I is the intrinsic spin-orbit coupling, λ_{VZ} is the valley Zeeman spin-orbit coupling, and λ_R is the Rashba SOC.

TMDC	t (eV)	Δ (meV)	λ_R (meV)	λ_I (μeV)	λ_{VZ} (meV)
$MoSe_2$	2.53	−0.59	0.29	−3.87	0.28
WSe_2	2.531	−0.52	0.51	−3.06	1.15

uniform parameters of the Dirac Hamiltonian [52]:

$$\tilde{\lambda}_I^A = (\lambda_I + \lambda_{VZ}),$$
$$\tilde{\lambda}_I^B = (\lambda_I - \lambda_{VZ}),$$

where λ_I and λ_{VZ} are the intrinsic and VZ terms that can be thought of as the sublattice-symmetric and -asymmetric contributions to a Kane-Mele-type coupling. Note that there are additional terms in the proximitized graphene Hamiltonian, namely, $\mathcal{H}_{PIA}$ and $\mathcal{H}_{\Delta PIA}$, that are responsible for the renormalization of the Fermi velocity and spin-dependent band splitting further from the valleys [60]. However, since their contribution to the low-energy electronic behavior close to valleys is negligible compared to other SOC terms, they are not included in this study.

To model the interface modes in proximitized graphene, we consider a TMDC layer that is composed of $MoSe_2$ and WSe_2 domains, which should guarantee a crossover from normal to inverted bands and lead to the emergence of TPH states due to the switching sign of the valley Chern index. To allow for periodic boundary conditions, we consider a Gr/(Mo-W)Se_2 supercell with two interfaces between the Gr/WSe_2 and Gr/$MoSe_2$ regions, as shown in Fig. 1(a). Note that the exact system illustrated here is used only for DFT calculations, while for the TB simulations, we consider significantly larger, but schematically similar, supercells. We use the SOC parameters of Gr/$MoSe_2$ (Gr/WSe_2) detailed in Table I for carbon atoms located in the $MoSe_2$ (WSe_2) domain. Note that we do not include the sublattice-symmetric intrinsic SOC as it is significantly smaller than the other SOC parameters. Furthermore, we consider the interfaces aligned with the zigzag direction of the graphene lattice. As a result, the Dirac points are projected onto two distinct momenta, which prevents intervalley scattering that is detrimental to the interface modes [49]. Note that we present results for abrupt steplike transitions between the proximity SOCs of the neighboring domains; however, calculations with a smoothly changing SOC over the interfaces yield similar results.

III. ALLOYED AND INTERFACE STATES

Before considering large-scale TB simulations, we first consider a more atomically accurate DFT computation of a Gr/(Mo-W)Se_2 heterostructure using the QUANTUM ESPRESSO package [61]. We consider a supercell 3.4 nm wide with a commensurate 4:3 Gr/TMDC ratio structure. The supercell is equally divided into Gr/WSe_2 and Gr/$MoSe_2$ domains, as shown in Fig. 1(a). The details of DFT calculations can be found in the footnote [62]. The DFT calculated electronic dispersion of the Gr/(Mo-W)Se_2 heterostructure is illustrated in Fig. 1(c). The resulting band structure does not correspond directly to either the pure Gr/$MoSe_2$ [Fig. 1(b)] or Gr/WSe_2 [Fig. 1(d)] heterostructure and, furthermore, does not show the band gap closure or branch crossings indicative of localized interface modes. Instead, it closely resembles the band structure predicted by the effective WAVG model (dashed line), i.e., a Dirac model using the weighted average of the SOC parameters from each of the pure systems (see Table I) [52]. The electronic dispersion shows an inverted band regime, as expected for an alloyed Gr/$W_\chi Mo_{1-\chi} Se_2$ system with $\chi = 0.5$ [52]. Although we have distinct Mo and W domains in the system, the band dispersion is identical to that of an alloyed system with the same concentration of randomly distributed metal atoms. This also suggests a bulk band gap closure should be expected when the Mo region expands to 66% of the TMDC layer, as this is the critical concentration ratio in random alloys. The similarity between the DFT and effective WAVG models and the lack of interface states can be attributed to a strong overlap between the wave functions of the Gr/$MoSe_2$ and Gr/WSe_2 domains. This prevents states with different valley Chern indices from forming in each domain and suppresses interface states along the domain boundaries. However, we note here that the domains are relatively small compared to the Fermi wavelength dictated by the relevant energy scale, namely, the proximity-induced energy gap, which, from the continuum model Hamiltonian, is $\sim 2|\Delta + \lambda_{VZ}|$ [36], where Δ and λ_{VZ} are the magnitudes of the staggered on-site potential and VZ SOC parameter, respectively. Considering the weighted average model parameters for the band structure, the energy gap is approximately 0.3 meV, corresponding to a length scale of the order of $\lambda_F \sim 10\,\mu m$. Therefore, size effects suppress the boundary state features in the system considered here, where $d \ll \lambda_F$.

Our DFT results and simple scaling analysis suggest that interface states do not emerge at this system size, yet the valley Chern index analysis suggests that these states must eventually appear as the domain size is increased. We now address the question of when in-gap states appear and how the band structure evolves between the homogeneous effective medium and multiple domain regimes. We start with small Gr/(Mo-W)Se_2 systems and gradually enlarge the domain size so that states in each domain are less likely to interact. We note that, since the TB band structure agrees exactly with the DFT results [see Fig. 1(b)], we can use the computationally less expensive TB model discussed in Sec. II to evaluate the electronic structure of wider systems, where *ab initio* calculations are intractable. Figure 2 presents the low-energy dispersion of Gr/(Mo-W)Se_2 with different size domains (different columns). The leftmost column, showing the case with the smallest cell, also plots the band structure predicted by the WAVG effective medium model (symbols) alongside the TB bands (solid lines) for comparison. From Figs. 2(a)–2(d), we increase the domain size by a factor of 25, without any significant change to the TB band structures, which continue to exactly mimic the WAVG model. The emergent bands are not similar to those in pure $MoSe_2$ or WSe_2 domains [orange and cyan shaded regions in Fig. 2(d)], nor do they display any signatures of branch crossings which could indicate the

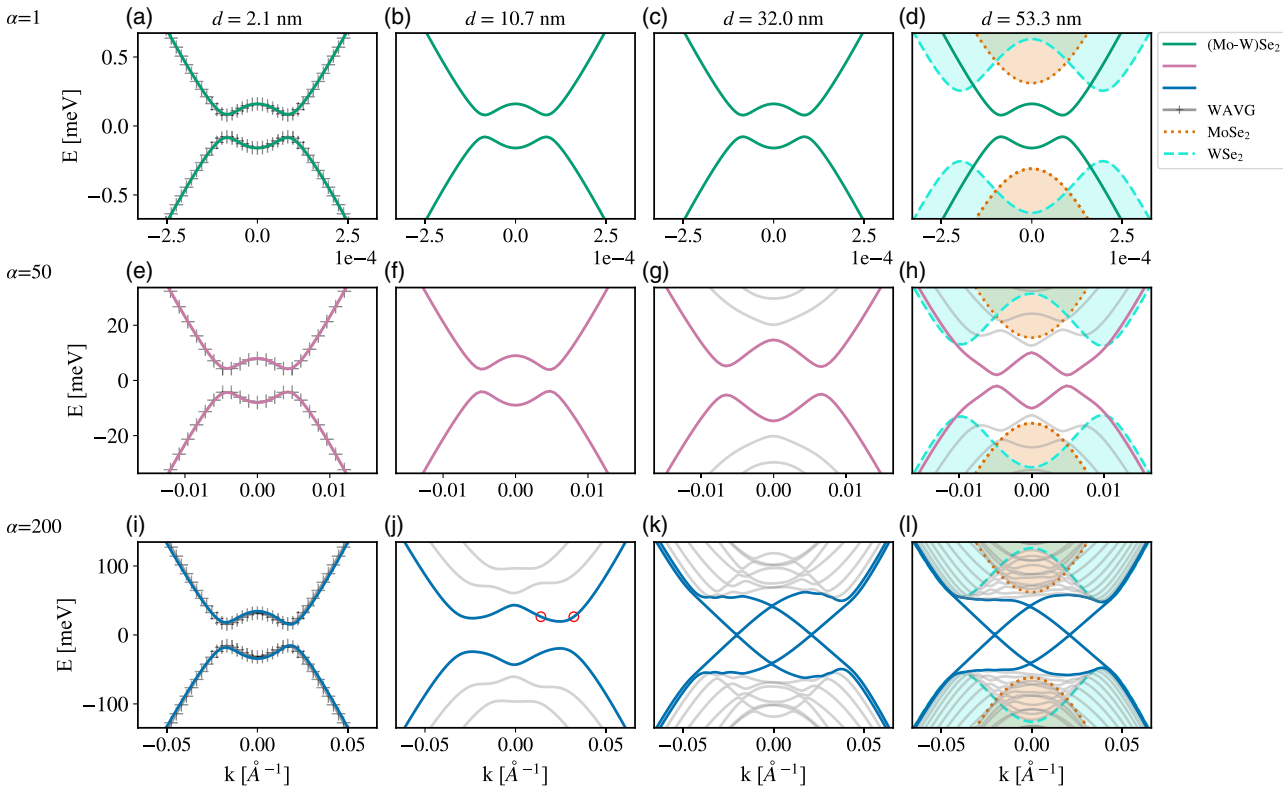

FIG. 2. The evolution of the electronic band structure of proximitized graphene with different SOC domains versus the SOC parameter and domain size. The outermost conduction and valence bands near the K valley are illustrated in dark green, purple, and blue to highlight the emergence of the interface states. The SOC parameters used are those of $Gr/MoSe_2$ and Gr/WSe_2 enhanced by a factor of (a)–(d) $\alpha = 1$ (not enhanced), (e)–(h) $\alpha = 50$, and (i)–(l) $\alpha = 200$. The WAVG model bands and those of a pristine Gr/TMDC heterostructure are depicted in the first and last columns for comparison. The lattice size is indicated at the top of each column. The open red circles in (j) are the specific states that will be used in Fig. 4 for real-space expansion of the wave functions.

emergence of localized interface modes [49]. Note that the domains here are still significantly smaller than the Fermi wavelength suggested by the energy gap scale in these systems. To examine regimes where the Fermi wavelength and system size become similar in magnitude, we now increase the magnitude of each of the proximity terms in the Hamiltonian by a factor $\alpha = 50$ (middle row) and $\alpha = 200$ (bottom row). This approach essentially renormalizes the energy and length scales and allows us to infer the physics of larger systems with realistic SOC parameters from that of smaller systems with enhanced SOC. For simplicity, we will continue to use the terminology $Gr/MoSe_2$ and Gr/WSe_2 to refer to the associated pristine systems with enhanced SOC, as the qualitative nature of the bands is unchanged. The validity of this approach will be discussed further in the next section. The smallest system cell for both α values [Figs. 2(e) and 2(i)] still perfectly follows the effective model band. However, as we move towards larger domain sizes with enhanced SOC, the bulk gap changes, and the bands evolve to form the in-gap states. As we increase the domain size for $\alpha = 200$ in Figs. 2(i)–2(l), we note an initial enhancement of the energy gap, before the gap eventually closes due to branch crossings in the energy dispersion. The four branches crossing at zero energy allude to the formation of interface modes, while the bulk bands closely follow those of pristine $Gr/MoSe_2$-type and Gr/WSe_2-type systems, as depicted by the shaded orange and cyan regions, respectively. The subgap states we find here are similar to those of a bilayer graphene with stacking registry domains in the presence of an external electric field [7,50] and also the domain wall modes in proximitized graphene with a sign-changing VZ term on a constant Rashba background [49]. The initial enhancement of the gap, visible, for example, in Fig. 2(j), is consistent with the fact that the gap for uniform $Gr/MoSe_2$-type and Gr/WSe_2-type systems is greater than that of the alloyed system. It can therefore be seen as a sign of the breakdown of alloyed-type behavior and the onset of individual domains with different electronic properties.

IV. SIZE EFFECTS

Figure 2 suggests that proximitized graphene can, indeed, host branch crossings and the associated interface states at the interface between regions with $MoSe_2$-type and WSe_2-type proximity SOCs. However, this was shown explicitly only for systems with a hugely enhanced SOC, $\alpha = 200$, so it is worth examining the agreement between systems with different lengths and energy scales more closely. In particular, it is important to determine the domain size that would be required for interface states to emerge in a real $Gr/(Mo\text{-}W)Se_2$ heterostructure, i.e., $\alpha = 1$.

In the simplest Dirac model for graphene, the inverse scaling relationship between length L and energy E is perfect: the

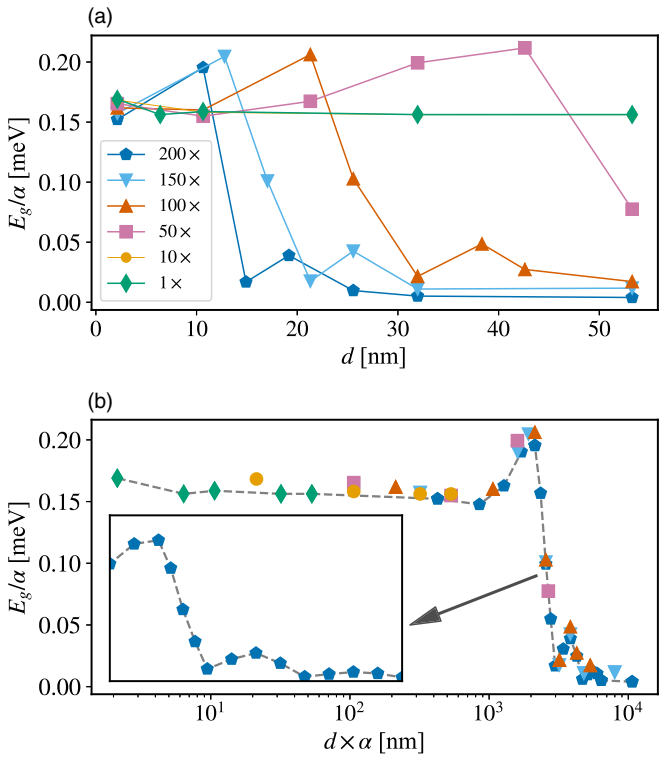

FIG. 3. (a) Energy gaps for Gr/(Mo-W)Se_2 as a function of domain size, normalized by the enhancement factor $\alpha = \{1, 10, 50, 100, 150, 200\}$ of the proximity SOC parameters in the Gr/$MoSe_2$ and Gr/WSe_2 domains. (b) is an exact replica of (a), except that the domains are enhanced by α for better comparison between the different structures. The inset shows zoomed-in oscillations of the energy gap for $\alpha = 200$.

mathematical description is identical if $E \to \alpha E$ and $L \to \frac{L}{\alpha}$. However, this is not guaranteed for more complicated dispersion relations or in TB descriptions, where the scale of the SOC parameters compared to the hopping integral also plays a role. It is therefore important to establish that similar behavior is found across the different energy and length scales considered in Fig. 2. One way to tackle this issue is to compare the band gap evolution as a function of both the domain size and the magnitude of the SOC terms. Band gap closure is a clear fingerprint of the establishment of branch crossings in the electronic structure, as shown in Fig. 2, so the band gap evolution is a suitable metric to ensure the same behavior is expected across different scales.

Figure 3(a) shows the energy gaps for Gr/(Mo-W)Se_2 as a function of domain size, normalized by the enhancement factor α of the proximity SOC parameters in the Gr/$MoSe_2$ and Gr/WSe_2 regions. Alongside the values in Fig. 2, we also consider a range of intermediate values and show here results for $\alpha = \{1, 10, 50, 100, 150, 200\}$. The convergence of the curves for different SOC strengths at small d shows that random alloy behavior emerges for all cases, as expected, in the limit of very small domains. This effective medium regime also persists across all the domain sizes considered for small values of α, which is evident from the constant band gaps for the $\alpha = 1$ and $\alpha = 10$ curves. However, for larger values of α, a nonmonotonic evolution of the band gap is observed. The dark blue $\alpha = 200$ curve corresponds to the bottom row of Fig. 2 and shows the initial increase and eventual suppression of the band gap as the domain size increases. Similar behavior is noted for the $\alpha = 50, 100, 150$ curves, but with a shift towards larger domain sizes for smaller SOC parameters, as expected.

To determine whether the band gap evolution is universal across different scales, in Fig. 3(b), we plot the band gaps found for a wide range of d combinations. In this plot, we also rescale the domain size according to the value of α used in the calculation and find that all the different cases in Fig. 3(b) now lie on a single "master" curve (dashed line). This confirms that the simple inverse scaling relationship between energy and size holds for proximitized graphene. We note this can be explained by the fact that although the SOC parameters are enhanced by up to two orders of magnitude, they are still significantly smaller than the magnitude of the hopping integral (∼3 eV) in graphene and the resultant gaps are formed well within the linear regime of the graphene dispersion relation. The robustness of this scaling also allows us to predict the domain size required for band gap closure and the emergence of branch crossings in real Gr/(Mo-W)Se_2 heterostructures. The smallest domain size required in this case is approximately 4 μm, which we note corresponds closely to the domain sizes achieved in chemical vapor deposition grown $MoSe_2/WSe_2$ lateral heterostructures [53].

Finally, we note that the band gap closure for larger system sizes does not occur as a simple decay, but instead, a superimposed oscillation occurs, which is shown more clearly in the inset of Fig. 3(b) for the $\alpha = 200$ case. This behavior is similar to the size-dependent oscillatory transition from the pseudohelical to insulating regime in Gr/WSe_2 nanoribbons reported before [47]. This is consistent with long-range coupling between localized states at neighboring interfaces, similar to the Ruderman-Kittel-Kasuya-Yosida (RKKY) interaction that can occur between magnetic impurities [63–65] or defect lines [66] in graphene. A decay rate of $\sim d^{-2.7}$ is extracted from the band gaps shown here, which is consistent with the expected decays of between d^{-2} and d^{-3} predicted for different RKKY scenarios in graphene.

V. INTERFACE STATES

Proximity to either $MoSe_2$ and WSe_2 breaks inversion symmetry and leads to sharp peaks in the momentum-space Berry curvatures around the K and K' valleys in the energy dispersion of graphene. The proximitized Hamiltonian thus gives rise to nonzero Chern indices in the individual valleys. However, as a result of the unbroken time-reversal symmetry, these valley Chern indices are not independent due to the vanishing total Chern number and cannot be regarded as a robust topological order [46]. Nevertheless, at the interfaces of domains with different valley Hall conductivities, robust one-dimensional states form; however, they are not topologically protected against any perturbation that couples the valleys, i.e., intervalley scattering processes. In the absence of such scattering, the number of one-dimensional channels per valley at such an interface is equal to the difference between their valley Chern indices, i.e., $C_V = C_K - C_{K'}$. This is in contrast

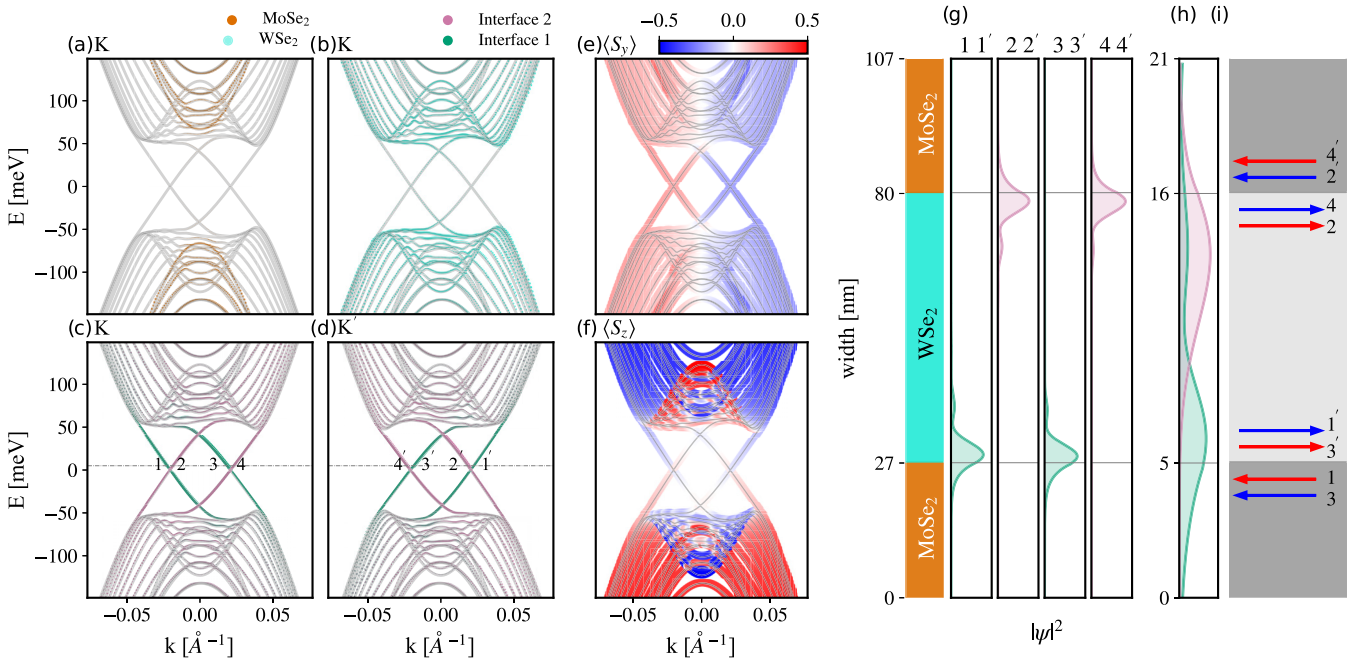

FIG. 4. Different domains, i.e., (a) Gr/MoSe2 and (b) Gr/WSe2, and interface contributions to eigenvalue weight in proximitized graphene with an approximate width of 107 nm around the (c) K and (d) K' valleys. The SOC parameters of $MoSe_2$ and WSe_2 are enhanced by a factor of 200. The contributions of the first and second interfaces are depicted in green and purple. (e) and (f) The spin textures along the in-plane (y) and transverse (z) axes. The band colors indicate the spin projection. (g) The real-space expansion of the interface states at momentum values where the dashed lines in (c) and (d) cross the lowest conduction band. The colors correspond to the interface at which the in-gap states are localized. (h) Real-state distribution of the wave functions for a 21 nm cell system at k values indicated by the open red circles in Fig. 2(j). The solid lines in (g) and (h) depict the interfaces' location in the cell. (i) Schematic illustration of in-gap states propagating along the Mo/W interfaces in the K and K' valleys. The labels correspond to the energy levels depicted in (c) and (d). The colors for the in-gap states show the spin projection along the y axis.

to the quantum spin Hall effect (QSHE), where the presence and the number of helical states are determined by the bulk Chern invariant. Therefore, the interface modes do not share the same origin as the helical states observed in the QSHE. Since $C_V = -1$ for $Gr/MoSe_2$ and $C_V = 1$ for Gr/WSe_2, we expect two pairs of boundary states for each interface in the system.

Since our supercell has two interfaces, we therefore expect four branch crossings in total per valley, consistent with what is observed in, for example, Fig. 2(l). We now need to confirm that band structure indeed corresponds to a superposition of $Gr/MoSe_2$- and Gr/WSe_2-type gapped bulk bands in their respective domains and gapless modes along the interfaces between them. This can be seen by analyzing the eigenvector weights in different regions of the supercell. The contributions of $MoSe_2$ (orange), WSe_2 (cyan), the first interface (interface 1, green), and the second interface (interface 2, purple) to the heterostructure dispersion near the K point are shown by the colored symbols in Figs. 4(a)–4(c). The bulk bands can clearly be seen to be a combination of independent $Gr/MoSe_2$-type [Fig. 4(a)] and Gr/WSe_2-type [Fig. 4(b)] bands, each largely confined to its own domain. For example, Fig. 4(a) shows that the outermost, inverted subbands, which are a defining feature of the pure Gr/WSe_2 system, have no weight in $Gr/MoSe_2$ regions. Meanwhile, the low-energy branch crossings, numbered 1–4 in Fig. 4(c), are strongly localized along the two interfaces in the supercell. Furthermore, we see the expected number of crossings at each interface with the propagation direction of interface modes swapped in the K' valley [Fig. 4(d)] due to time-reversal symmetry.

The spatial localization of the interface branch modes is shown in more detail in Fig. 4(g), where we plot the eigenvector weight as a function of position for each of the branch crossings numbered in Figs. 4(c) and 4(d). The modes present at each interface, together with their propagation direction and spin orientation, are shown in Fig. 4(i). In each valley, there are two pairs of interface branches, which are localized at opposite interfaces and propagate in opposite directions. In the K valley, for example, modes 1 and 3 propagate from right to left along interface 1, whereas modes 2 and 4 propagate in the opposite direction along interface 2. Furthermore, rightward and leftward propagating in-gap modes, which are related to each of the K and K' valleys, are spatially separated and localized at different interfaces, resulting in a valley filtering phenomenon. Figures 4(e) and 4(f) show the spin textures of the low-energy states along the in-plane (y) and out-of-plane (z) directions, respectively. Unlike the edge modes in the simplest QSHE case [19], the low-energy interface modes here have largely in-plane spin polarizations, with only a smaller component in the z direction due to the presence of the Rashba term in the proximity SOC. We have colored the arrows in Fig. 4(i) according to the larger, in-plane polarization of each mode. Note that it is the valley and not the spin index which determines the propagation direction of boundary states. The interfaces in this system can be viewed as hosting two instances of the QVHE, one for each of two spin orientations.

As such, transport in the interface modes is protected against backscattering in the absence of intervalley scattering.

For smaller domains, the wave functions of counterpropagating modes from neighboring interfaces can overlap, as shown in Fig. 4(h) for the $d = 10.7$ nm case. Here, the low-energy states are delocalized over the entire graphene lattice and do not give rise to well-defined interface states. The resultant hybridization opens a gap in the corresponding band structure, which is shown in Fig. 2(j). On the other hand, when the domains become large enough to prevent overlap, as shown in Fig. 4(g), the interface modes emerge, and the gap in the band structure closes.

Finally, we note that in systems where the interfaces are oriented along the armchair direction, the K and K' valleys are folded onto the same point in the reciprocal space. However, similar to previous studies [18,49,50], our calculations show that this does not lead to the annihilation of the interface states. Only in the presence of a sharp transition between the different valley Hall effect regions does a small bulk gap open, but as the transition becomes smoother, the gap vanishes. As a result, in the absence of intervalley scattering, the interface states protected by time-reversal symmetry are particularly resilient to orientational faults. This is especially important because it may be difficult to achieve precise alignment between the TMDC interface and the graphene zigzag direction in heterostructures fabricated using dry transfer methods.

VI. CONCLUSIONS

Proximity to TMDCs can lead to the emergence of TPH states in graphene similar to those predicted by Kane and Mele when spin-orbit interactions are included. These interactions are rather complex and consist of different induced coupling mechanisms in the low-energy spectrum. The SOC in proximitized graphene involves a substrate-induced Rashba term that couples electrons of different spin orientations, the intrinsic term that induces a topological gap, and the sublattice-asymmetric VZ term that couples the spin and valleys. In contrast to the Kane-Mele model, however, the staggered intrinsic SOC in Gr/TMDC yields a trivial topological order, with nonzero Berry curvature and hence a nonzero Chern index at individual valleys. In this work, we studied the cases of $Gr/MoSe_2$, with a direct optical band gap, and Gr/WSe_2, with VZ-driven inverted bands, since they can act as an interesting platform for the realization of TPH states by enabling a topological crossover with band gap closure when placed together in a composite system. We demonstrated the emergence of the localized boundary states in a $Gr/(Mo\text{-}W)Se_2$ heterostructure where W- and Mo-like domains with opposite valley Chern indices are formed. These interface states are analogous to gapless chiral edge states in the quantum spin Hall regime, except that the valley degree of freedom plays the role of the spin. Utilizing a microscopic study, we showed how topologically protected in-gap modes evolve with the lattice size and how they can hybridize to a weighted average effective model state similar to a randomized composite system when the domains are remarkably smaller than the Fermi wavelength.

ACKNOWLEDGMENTS

The authors acknowledge the support of the Irish Centre for High-End Computing (ICHEC). This study is funded by the Irish Research Council under the Laureate awards and the Government of Ireland postdoctoral fellowship program.

[1] M. Zarenia, J. M. Pereira, Jr., G. A. Farias, and F. M. Peeters, Chiral states in bilayer graphene: Magnetic field dependence and gap opening, Phys. Rev. B **84**, 125451 (2011).

[2] Z. Qiao, J. Jung, Q. Niu, and A. H. MacDonald, Electronic highways in bilayer graphene, Nano Lett. **11**, 3453 (2011).

[3] J. Klinovaja, G. J. Ferreira, and D. Loss, Helical states in curved bilayer graphene, Phys. Rev. B **86**, 235416 (2012).

[4] O. Shevtsov, P. Carmier, C. Petitjean, C. Groth, D. Carpentier, and X. Waintal, Graphene-Based Heterojunction between Two Topological Insulators, Phys. Rev. X **2**, 031004 (2012).

[5] L. Ju, Z. Shi, N. Nair, Y. Lv, C. Jin, J. Velasco Jr, C. Ojeda-Aristizabal, H. A. Bechtel, M. C. Martin, A. Zettl, J. Analytis, and F. Wang, Topological valley transport at bilayer graphene domain walls, Nature (London) **520**, 650 (2015).

[6] J. Li, K. Wang, K. J. McFaul, Z. Zern, Y. Ren, K. Watanabe, T. Taniguchi, Z. Qiao, and J. Zhu, Gate-controlled topological conducting channels in bilayer graphene, Nat. Nanotechnol. **11**, 1060 (2016).

[7] L.-J. Yin, H. Jiang, J.-B. Qiao, and L. He, Direct imaging of topological edge states at a bilayer graphene domain wall, Nat. Commun. **7**, 11760 (2016).

[8] B. Tsim, N. N. T. Nam, and M. Koshino, Perfect one-dimensional chiral states in biased twisted bilayer graphene, Phys. Rev. B **101**, 125409 (2020).

[9] Y. H. Kwan, G. Wagner, N. Chakraborty, S. H. Simon, and S. A. Parameswaran, Domain wall competition in the Chern insulating regime of twisted bilayer graphene, Phys. Rev. B **104**, 115404 (2021).

[10] P. San-Jose and E. Prada, Helical networks in twisted bilayer graphene under interlayer bias, Phys. Rev. B **88**, 121408(R) (2013).

[11] S. Huang, K. Kim, D. K. Efimkin, T. Lovorn, T. Taniguchi, K. Watanabe, A. H. MacDonald, E. Tutuc, and B. J. LeRoy, Topologically Protected Helical States in Minimally Twisted Bilayer Graphene, Phys. Rev. Lett. **121**, 037702 (2018).

[12] P. Rickhaus, J. Wallbank, S. Slizovskiy, R. Pisoni, H. Overweg, Y. Lee, M. Eich, M.-H. Liu, K. Watanabe, T. Taniguchi, T. Ihn, and K. Ensslin, Transport through a network of topological channels in twisted bilayer graphene, Nano Lett. **18**, 6725 (2018).

[13] H. Yoo, R. Engelke, S. Carr, S. Fang, K. Zhang, P. Cazeaux, S. H. Sung, R. Hovden, A. W. Tsen, T. Taniguchi, K. Watanabe, G.-C. Yi, M. Kim, M. Luskin, E. B. Tadmor, E. Kaxiras, and

P. Kim, Atomic and electronic reconstruction at the van der Waals interface in twisted bilayer graphene, Nat. Mater. **18**, 448 (2019).

[14] I. V. Lebedeva and A. M. Popov, Energetics and structure of domain wall networks in minimally twisted bilayer graphene under strain, J. Phys. Chem. C **124**, 2120 (2020).

[15] D. K. Efimkin and A. H. MacDonald, Helical network model for twisted bilayer graphene, Phys. Rev. B **98**, 035404 (2018).

[16] I. Martin, Y. M. Blanter, and A. F. Morpurgo, Topological Confinement in Bilayer Graphene, Phys. Rev. Lett. **100**, 036804 (2008).

[17] W. Yao, S. A. Yang, and Q. Niu, Edge States in Graphene: From Gapped Flat-Band to Gapless Chiral Modes, Phys. Rev. Lett. **102**, 096801 (2009).

[18] J. Jung, F. Zhang, Z. Qiao, and A. H. MacDonald, Valley-Hall kink and edge states in multilayer graphene, Phys. Rev. B **84**, 075418 (2011).

[19] C. L. Kane and E. J. Mele, Quantum Spin Hall Effect in Graphene, Phys. Rev. Lett. **95**, 226801 (2005).

[20] C. L. Kane and E. J. Mele, Z_2 Topological Order and the Quantum Spin Hall Effect, Phys. Rev. Lett. **95**, 146802 (2005).

[21] A. Avsar, J. Y. Tan, T. Taychatanapat, J. Balakrishnan, G. Koon, Y. Yeo, J. Lahiri, A. Carvalho, A. Rodin, E. O'Farrell, G. Eda, A. H. Castro Neto, and B. Özyilmaz, Spin–orbit proximity effect in graphene, Nat. Commun. **5**, 4875 (2014).

[22] W. Han, R. K. Kawakami, M. Gmitra, and J. Fabian, Graphene spintronics, Nat. Nanotechnol. **9**, 794 (2014).

[23] Z. Wang, D.-K. Ki, H. Chen, H. Berger, A. H. MacDonald, and A. F. Morpurgo, Strong interface-induced spin–orbit interaction in graphene on WS_2, Nat. Commun. **6**, 8339 (2015).

[24] Z. Wang, D.-K. Ki, J. Y. Khoo, D. Mauro, H. Berger, L. S. Levitov, and A. F. Morpurgo, Origin and Magnitude of 'Designer' Spin-Orbit Interaction in Graphene on Semiconducting Transition Metal Dichalcogenides, Phys. Rev. X **6**, 041020 (2016).

[25] J. H. Garcia, A. W. Cummings, and S. Roche, Spin Hall effect and weak antilocalization in graphene/transition metal dichalcogenide heterostructures, Nano Lett. **17**, 5078 (2017).

[26] T. S. Ghiasi, J. Ingla-Aynés, A. A. Kaverzin, and B. J. van Wees, Large proximity-induced spin lifetime anisotropy in transition-metal dichalcogenide/graphene heterostructures, Nano Lett. **17**, 7528 (2017).

[27] A. Dankert and S. P. Dash, Electrical gate control of spin current in van der Waals heterostructures at room temperature, Nat. Commun. **8**, 16093 (2017).

[28] A. L. Friedman, K. M. McCreary, J. T. Robinson, O. M. van 't Erve, and B. T. Jonker, Spin relaxation and proximity effect in WS_2/graphene/fluorographene non-local spin valves, Carbon **131**, 18 (2018).

[29] T. Wakamura, F. Reale, P. Palczynski, S. Guéron, C. Mattevi, and H. Bouchiat, Strong Anisotropic Spin-Orbit Interaction Induced in Graphene by Monolayer WS_2, Phys. Rev. Lett. **120**, 106802 (2018).

[30] L. A. Benítez, J. F. Sierra, W. Savero Torres, A. Arrighi, F. Bonell, M. V. Costache, and S. O. Valenzuela, Strongly anisotropic spin relaxation in graphene–transition metal dichalcogenide heterostructures at room temperature, Nat. Phys. **14**, 303 (2018).

[31] M. Offidani and A. Ferreira, Microscopic theory of spin relaxation anisotropy in graphene with proximity-induced spin-orbit coupling, Phys. Rev. B **98**, 245408 (2018).

[32] J. O. Island, X. Cui, C. Lewandowski, J. Y. Khoo, E. M. Spanton, H. Zhou, D. Rhodes, J. C. Hone, T. Taniguchi, K. Watanabe, L. S. Levitov, M. P. Zaletel, and A. F. Young, Spin-orbit-driven band inversion in bilayer graphene by the van der Waals proximity effect, Nature (London) **571**, 85 (2019).

[33] A. David, P. Rakyta, A. Kormányos, and G. Burkard, Induced spin-orbit coupling in twisted graphene-transition metal dichalcogenide heterobilayers: Twistronics meets spintronics, Phys. Rev. B **100**, 085412 (2019).

[34] H. S. Arora, R. Polski, Y. Zhang, A. Thomson, Y. Choi, H. Kim, Z. Lin, I. Z. Wilson, X. Xu, J.-H. Chu, K. Watanabe, T. Taniguchi, J. Alicea, and S. Nadj-Perge, Superconductivity in metallic twisted bilayer graphene stabilized by WSe_2, Nature (London) **583**, 379 (2020).

[35] H. Min, J. E. Hill, N. A. Sinitsyn, B. R. Sahu, L. Kleinman, and A. H. MacDonald, Intrinsic and Rashba spin-orbit interactions in graphene sheets, Phys. Rev. B **74**, 165310 (2006).

[36] M. Gmitra, D. Kochan, P. Högl, and J. Fabian, Trivial and inverted Dirac bands and the emergence of quantum spin Hall states in graphene on transition-metal dichalcogenides, Phys. Rev. B **93**, 155104 (2016).

[37] B. Yang, M.-F. Tu, J. Kim, Y. Wu, H. Wang, J. Alicea, R. Wu, M. Bockrath, and J. Shi, Tunable spin–orbit coupling and symmetry-protected edge states in graphene/WS_2, 2D Mater. **3**, 031012 (2016).

[38] W. Yan, O. Txoperena, R. Llopis, H. Dery, L. E. Hueso, and F. Casanova, A two-dimensional spin field-effect switch, Nat. Commun. **7**, 13372 (2016).

[39] T. Völkl, T. Rockinger, M. Drienovsky, K. Watanabe, T. Taniguchi, D. Weiss, and J. Eroms, Magnetotransport in heterostructures of transition metal dichalcogenides and graphene, Phys. Rev. B **96**, 125405 (2017).

[40] J. F. Sierra, J. Fabian, R. K. Kawakami, S. Roche, and S. O. Valenzuela, van der Waals heterostructures for spintronics and opto-spintronics, Nat. Nanotechnol. **16**, 856 (2021).

[41] P. Tiwari, S. K. Srivastav, and A. Bid, Electric-Field-Tunable Valley Zeeman Effect in Bilayer Graphene Heterostructures: Realization of the Spin-Orbit Valve Effect, Phys. Rev. Lett. **126**, 096801 (2021).

[42] A. W. Cummings, J. H. Garcia, J. Fabian, and S. Roche, Giant Spin Lifetime Anisotropy in Graphene Induced by Proximity Effects, Phys. Rev. Lett. **119**, 206601 (2017).

[43] B. Yang, M. Lohmann, D. Barroso, I. Liao, Z. Lin, Y. Liu, L. Bartels, K. Watanabe, T. Taniguchi, and J. Shi, Strong electron-hole symmetric Rashba spin-orbit coupling in graphene/monolayer transition metal dichalcogenide heterostructures, Phys. Rev. B **96**, 041409(R) (2017).

[44] J. H. Garcia, M. Vila, A. W. Cummings, and S. Roche, Spin transport in graphene/transition metal dichalcogenide heterostructures, Chem. Soc. Rev. **47**, 3359 (2018).

[45] J. Ingla-Aynés, F. Herling, J. Fabian, L. E. Hueso, and F. Casanova, Electrical Control of Valley-Zeeman Spin-Orbit-Coupling–Induced Spin Precession at Room Temperature, Phys. Rev. Lett. **127**, 047202 (2021).

[46] A. M. Alsharari, M. M. Asmar, and S. E. Ulloa, Topological phases and twisting of graphene on a dichalcogenide monolayer, Phys. Rev. B **98**, 195129 (2018).

[47] T. Frank, P. Högl, M. Gmitra, D. Kochan, and J. Fabian, Protected Pseudohelical Edge States in $\mathbb{Z}_2$-Trivial Proximitized Graphene, Phys. Rev. Lett. **120**, 156402 (2018).

[48] A. M. Alsharari, M. M. Asmar, and S. E. Ulloa, Mass inversion in graphene by proximity to dichalcogenide monolayer, Phys. Rev. B **94**, 241106(R) (2016).

[49] J.-B. Touchais, P. Simon, and A. Mesaros, Robust propagating in-gap modes due to spin-orbit domain walls in graphene, Phys. Rev. B **106**, 035139 (2022).

[50] A. Vaezi, Y. Liang, D. H. Ngai, L. Yang, and E.-A. Kim, Topological Edge States at a Tilt Boundary in Gated Multilayer Graphene, Phys. Rev. X **3**, 021018 (2013).

[51] F. Zhang, A. H. MacDonald, and E. J. Mele, Valley Chern numbers and boundary modes in gapped bilayer graphene, Proc. Natl. Acad. Sci. USA **110**, 10546 (2013).

[52] Z. Khatibi and S. R. Power, Proximity spin-orbit coupling in graphene on alloyed transition metal dichalcogenides, Phys. Rev. B **106**, 125417 (2022).

[53] P. K. Sahoo, S. Memaran, Y. Xin, L. Balicas, and H. R. Gutiérrez, One-pot growth of two-dimensional lateral heterostructures via sequential edge-epitaxy, Nature (London) **553**, 63 (2018).

[54] X. Liu and M. C. Hersam, Interface characterization and control of 2D materials and heterostructures, Adv. Mater. **30**, 1801586 (2018).

[55] B. Zheng, C. Ma, D. Li, J. Lan, Z. Zhang, X. Sun, W. Zheng, T. Yang, C. Zhu, G. Ouyang, G. Xu, X. Zhu, X. Wang, and A. Pan, Band alignment engineering in two-dimensional lateral heterostructures, J. Am. Chem. Soc. **140**, 11193 (2018).

[56] P. K. Sahoo, S. Memaran, F. A. Nugera, Y. Xin, T. Díaz Márquez, Z. Lu, W. Zheng, N. D. Zhigadlo, D. Smirnov, L. Balicas, and H. Rodríguez Gutiérrez, Bilayer lateral heterostructures of transition-metal dichalcogenides and their optoelectronic response, ACS Nano **13**, 12372 (2019).

[57] S. Wang, X. Cui, C. Jian, H. Cheng, M. Niu, J. Yu, J. Yan, and W. Huang, Stacking-engineered heterostructures in transition metal dichalcogenides, Adv. Mater. **33**, 2005735 (2021).

[58] F. A. Nugera, P. K. Sahoo, Y. Xin, S. Ambardar, D. V. Voronine, U. J. Kim, Y. Han, H. Son, and H. R. Gutiérrez, Bandgap engineering in 2D lateral heterostructures of transition metal dichalcogenides via controlled alloying, Small **18**, 2106600 (2022).

[59] Y. Zuo *et al.*, Robust growth of two-dimensional metal dichalcogenides and their alloys by active chalcogen monomer supply, Nat. Commun. **13**, 1007 (2022).

[60] D. Kochan, S. Irmer, and J. Fabian, Model spin-orbit coupling Hamiltonians for graphene systems, Phys. Rev. B **95**, 165415 (2017).

[61] P. Giannozzi, S. Baroni, N. Bonini, M. Calandra, R. Car, C. Cavazzoni, D. Ceresoli, G. L. Chiarotti, M. Cococcioni, and I. Dabo, QUANTUM ESPRESSO: A modular and open-source software project for quantum simulations of materials, J. Phys.: Condens. Matter **21**, 395502 (2009).

[62] We employ fully relativistic projector augmented wave pseudopotentials in combination with the generalized gradient approximation (Perdew-Burke-Ernzerhof) for the exchange-correlation potential. We set the kinetic energy cutoff to 60 Ry and sample the Brillouin zone with $6\times6\times1$ k points. We optimize the atomic positions using the quasi-Newton algorithm based on the trust radius procedure. The adjacent layers interact via the weak van der Waals forces within a semiempirical approach [67]. Coulomb truncation is used [68], and a vacuum space of 13 Å is set to avoid the interactions between the images of the supercell along the transverse direction.

[63] M. A. H. Vozmediano, M. P. López-Sancho, T. Stauber, and F. Guinea, Local defects and ferromagnetism in graphene layers, Phys. Rev. B **72**, 155121 (2005).

[64] S. Saremi, RKKY in half-filled bipartite lattices: Graphene as an example, Phys. Rev. B **76**, 184430 (2007).

[65] S. R. Power and M. S. Ferreira, Indirect exchange and Ruderman–Kittel–Kasuya–Yosida (RKKY) interactions in magnetically-doped graphene, Crystals **3**, 49 (2013).

[66] P. D. Gorman, J. M. Duffy, S. R. Power, and M. S. Ferreira, RKKY interaction between extended magnetic defect lines in graphene, Phys. Rev. B **90**, 125411 (2014).

[67] S. Grimme, Semiempirical GGA-type density functional constructed with a long-range dispersion correction, J. Comput. Chem. **27**, 1787 (2006).

[68] T. Sohier, M. Calandra, and F. Mauri, Density functional perturbation theory for gated two-dimensional heterostructures: Theoretical developments and application to flexural phonons in graphene, Phys. Rev. B **96**, 075448 (2017).